Available online at www.sciencedirect.com
ScienceDirect
International Journal of Heat and Fluid Flow 29 (2008) 1089–1102
International Journal of HEAT AND FLUID FLOW
www.elsevier.com/locate/ijhff

Vortex dynamics in confined counter-current shearing flows with applications to mixing

Joseph A.C. Humphrey [a,*], Jorge L. Rosales [b], Lindsay A. Legendre [c], J. Patrick LeDuc [c], James P. Landers [c]

[a] Department of Mechanical and Aerospace Engineering, University of Virginia, 122 Engineer's Way, Charlottesville, VA 22904-4746, United States
[b] Phoenix Analysis and Design Technologies, ASU Research Park, 7755 S. Research Dr., Suite 110, Tempe, AZ 85284-1803, United States
[c] Department of Chemistry, University of Virginia, McCormick Road, Charlottesville, VA 22904-4319, United States

Received 29 October 2007; received in revised form 4 January 2008; accepted 4 February 2008
Available online 26 March 2008

Abstract

A numerical investigation has been performed for the time-dependent motion of a constant property, Newtonian fluid in a counter-current shearing flows configuration. In the geometry of interest, two initially separated streams are made to flow counter to each other at bulk average velocities U_1 and U_2 along the streamwise (x-coordinate) direction through a pair of stacked, straight, parallel channels. The channels have width W, height $H/2$ and length L, and are separated by a pair of thin plates with a discontinuity in length L_m centered at $L/2$. The counter-flowing streams interact dynamically in the space shared by the two channels, defined by the discontinuity between plates. This problem consists of a very simple Cartesian geometry with well posed initial and boundary conditions and yet, for the conditions explored, the resulting physics is highly non-linear and complex. Starting from rest, the counter-flowing streams in the shared space region initially display the characteristics of a two-dimensional saddle point flow when observed along the spanwise (z-coordinate) direction. Soon thereafter, depending on the shapes of the velocity profiles imposed at the channel inlet planes and the respective Reynolds numbers of the opposing streams $\left(Re_{1,2} \equiv \frac{U_{1,2}H/2}{\nu}\right)$, two pairs of vortices aligned in the transverse (y-coordinate) direction appear that can be stable or unstable. If the inlet plane velocity profiles are symmetric and $Re_1 = Re_2 = 300$ or $Re_1 = 2 \times Re_2 = 300$ each of the two channel vortex pairs counter-rotates and they are stable over long periods of time. If, however, the inlet velocity profiles are anti-symmetric one pair of anti-symmetric co-rotating vortices dominates the flow and they orbit around each other. For this case, if $Re_1 = Re_2 < 200$ the vortex pair merge and the resulting vortex structure is stable. In contrast, if $Re_1 = Re_2 > 200$, in the presence of stretching by the background saddle point flow the merging of the vortex pair is unstable and the resulting vortex structure ultimately collapses in a temporary burst of complex, three-dimensional, unsteady motion. Soon thereafter, the formation, merging and collapse of this vortex pair repeats. Aside from their intrinsic fundamental interest, the phenomena observed have potential applications for the controlled mixing of fluid streams at both low and high Reynolds numbers. Flow visualization results show how this can be achieved in a device consisting of a number of basic counter-current flow units concatenated in series.

Keywords: Vortex dynamics; Counter-current flows; Mixing

1. The problem of interest

In an earlier study, Humphrey and Li (1981) reported dye visualization observations revealing the time-evolving characteristics of pairs of transversely aligned vortices in a confined counter-current shearing flows configuration. With reference to Fig. 1, the basic flow geometry consists of two straight, stacked, parallel channels, each of width W, height $H/2$ ($= 0.76\,W$) and length $L = 2L_e + L_m$ ($= 5\,W$) through which a pair of oppositely directed water streams is made to flow after respectively passing through contracting inlet flow conditioning sections (not shown). The counter-flowing streams have bulk average velocities U_1 in the top channel and U_2 in the bottom, and corresponding

* Corresponding author. Tel.: +1 434 924 6213; fax: +1 434 982 2037.
E-mail address: jach@virginia.edu (J.A.C. Humphrey).

0142-727X/$ - see front matter © 2008 Elsevier Inc. All rights reserved.
doi:10.1016/j.ijheatfluidflow.2008.02.005

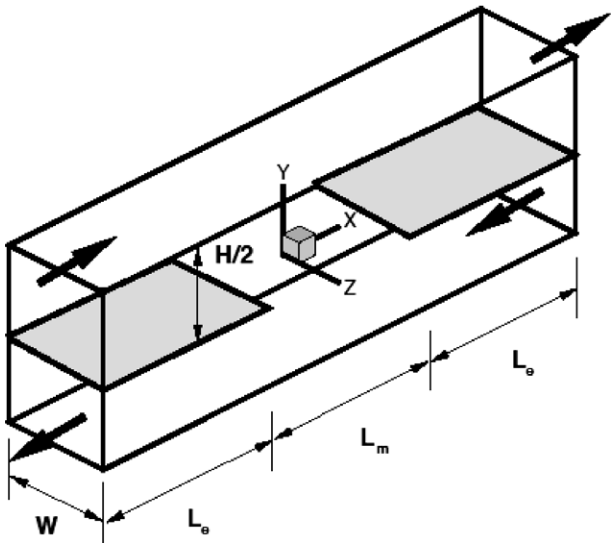

Fig. 1. Schematic of the calculation domain consisting of a pair of stacked channels separated by two splitter plates except for a section between them where the counter-flowing streams are allowed to shear. Most of the plots presented in this communication are for the flow in the shared space region defined by $L_m \times W \times H$.

Reynolds numbers $Re_{1,2} \equiv \frac{U_{1,2}H/2}{\nu}$, respectively. The streams are separated by a pair of thin metal plates with a discontinuity in length of magnitude L_m (=1.5 W) centered at $L/2$ that defines a shared space where they are allowed to interact. Figs. 2 and 3 show in color a sequence of flow visualization observations originally published in black and white by Humphrey and Li (1981). These authors found that for $Re_1 \approx Re_2$ motion starting from rest initially displayed a two-dimensional (2D) irrotational flow startup phase in the shared space region (Fig. 2a) with the characteristics of a saddle point. Then, for symmetrically shaped inlet plane velocity profile conditions, the transverse vortex pairs formed in the shared space region of the flow were observed to counter-rotate and be stable (Fig. 3a). However, for anti-symmetrically shaped inlet plane velocity profile conditions and sufficiently high values of the Reynolds numbers the transverse vortex pairs were observed to be unstable (Figs. 2b–d, and 3b–d). In this case, a dominant pair of anti-symmetric co-rotating vortices was observed to orbit around each other while being stretched by the background saddle point flow. Eventually, this pair of vortices merged and collapsed (Figs. 2b–d and 3b–d). The formation, merging and collapse of the dominant vortex pair was found to repeat at an average frequency that increased approximately linearly with increasing Reynolds numbers of the opposed channel flows.

An interesting feature of the experimental flow is that the merging and collapse of the anti-symmetric co-rotating vortex pair occurs at relatively low Reynolds numbers ($Re_1 \approx Re_2 = 400$–1000); see Humphrey and Li (1981). Yet the collapse of the vortices momentarily produces a rel-

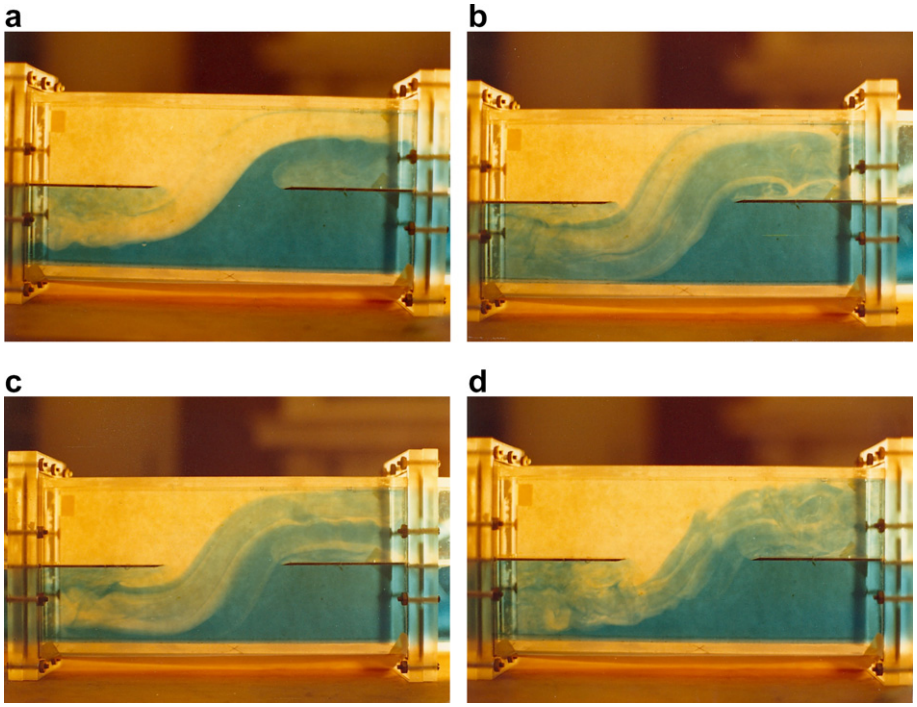

Fig. 2. Flow visualization results (x–y plane views) obtained by Humphrey and Li (1981) in the counter-current channel flows configuration shown in Fig. 1 for $Re_1 \approx Re_2 > 300$. Methylene blue colors the water stream entering the bottom channel at the right and, therefore, preferentially visualizes flow structures involving fluid from this stream. (a) Fluid motion starting from rest is initially 2D and irrotational in the shared space region, and the flow displays a saddle point character that remains present in the long term motion. (b–c) For anti-symmetric velocity profiles at the channel inlet planes, a pair of co-rotating vortices with intense ω_y component of vorticity dominates the flow in the shared space region. This pair of vortices orbit around each other, and eventually merge and collapse under the straining action of the saddle point flow (see Figs. 3b–d). The formation, merging and collapse of the vortex pair occurs at an average frequency that is proportional to the Reynolds number.

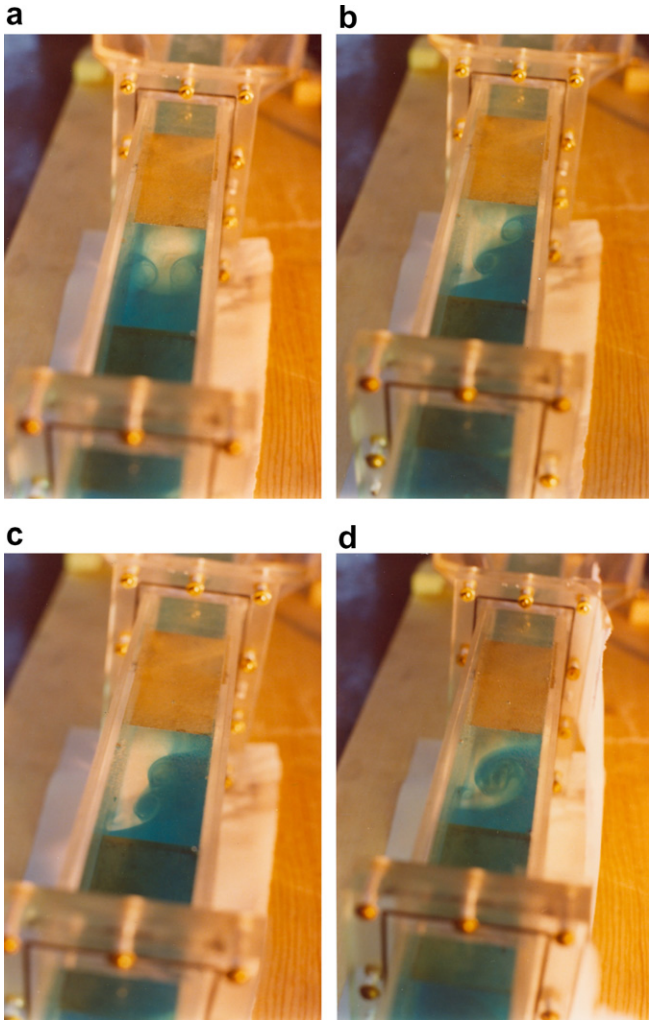

Fig. 3. Flow visualization results (x–z plane views) closely corresponding to the conditions of Fig. 2. (a) For symmetric velocity profiles at the channel inlet planes two pairs of stable counter-rotating vortices appear. (b–c) For anti-symmetric velocity profiles at the channel inlet planes, a pair of co-rotating vortices with intense ω_y component of vorticity dominates the flow in the shared space region. This pair of vortices orbit around each other, and eventually merge and collapse under the straining action of the saddle point flow (see Figs. 2b–d).

atively large range of energetic and disorganized scales of motion that help mix the counter-flowing streams in the shared space region. The questions arise, therefore, as to what are the dynamical characteristics of this low Reynolds number flow and whether they can be usefully applied to enhance mixing at low Reynolds numbers in ducted flow configurations which, otherwise, would be diffusion controlled.

The answers to these and related questions are of more than academic interest since they bear upon practical issues affecting the control of interacting fluid streams as well as their mixing. Thus, for example, Strykowski and his colleagues (Behrens et al., 2004; Forliti et al. 2004; 2005a,b; Lonnes et al., 2001) have demonstrated the use of counter-current shearing phenomena in various high Reynolds number flow combustor geometries. Similarly, in an investigation on the mixing at low Reynolds number of the flows through curved micro-passages, Sudarsan and Ugaz (2006) discuss the advantages of several mixing-enhancing features to overcome diffusion limited transport. These include the generation of cross-stream secondary flows as well as the splitting and recombination of fluid streams. Both of these features arise at all Reynolds numbers in the present flow configuration which, in addition, has the potential to further enhance mixing through the action of stable transverse vortices arising in the main flow or, for certain conditions, by the repeated generation, merging and collapse of these vortices to produce smaller, energetic, dispersing scales of motion.

In this investigation we present numerical results for the above counter-current flows configuration obtained using the Navier–Stokes solver of Rosales et al. (2000, 2001). Specifically, we investigate the formation and possible merging and collapse of transverse vortex pairs as a function of the shapes of the channel inlet velocity profiles and of the bulk average velocities through the channels. Emphasis is placed on analyzing the anti-symmetric inlet velocity profiles case for $Re_1 = Re_2 = 100$, 200 and 300. In general, we find that the calculations are in very good qualitative agreement with the earlier findings in Humphrey and Li (1981) for both stable and unstable flow conditions. Particularly interesting and new to this study are the detailed pictures that emerge concerning the formation, merging and collapse of the dominant vortex pair for anti-symmetric inlet plane velocity profile conditions. The numerical results obtained are of intrinsic fundamental value and suggest a possible method for enhancing and controlling the mixing of confined counter-flowing fluid streams at both low and high Reynolds numbers. The latter point is illustrated by reference to flow visualization results obtained in a device consisting of a number of basic counter-current flow units concatenated in series.

2. Preliminary considerations

Fig. 1 shows the flow calculation domain of interest. Except for the contracting inlet flow conditioning sections used in the experiment (not shown), it corresponds exactly to the geometry investigated by Humphrey and Li (1981) and consists of a pair of stacked channels of internal width $W = 5.08$ cm and total internal height $H = 7.7$ cm. Two splitter plates, each of thickness $t = 0.1$ cm and length $L_e = 8.9$ cm, separate the counter-flowing water streams. Thus, the height of each channel is $(H - t)/2 = 3.8$ cm. A discontinuity in the plates of length $L_m = 7.62$ cm defines a shared space region where the streams interact. One stream enters the top channel at the top-left in Fig. 1, and the other enters the bottom channel at the bottom-right. The streams flowing through each channel split in two in the shared space region. Here, part of the stream from one channel continues flowing along its length while the other part curves around the edge of the splitter plate to merge with the part of the opposing stream that contin-

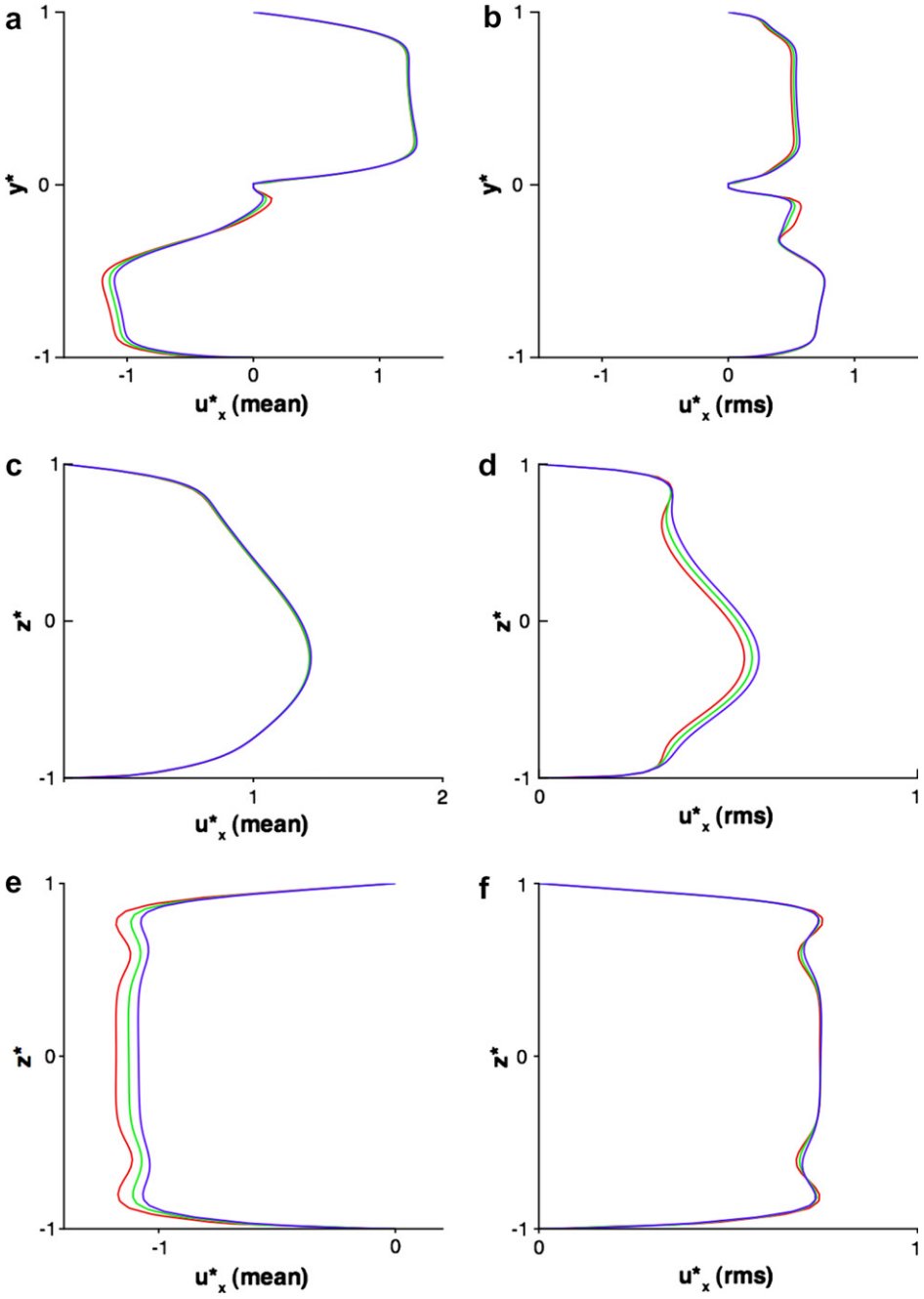

Fig. 4. Grid refinement results for Case 3 with $Re_1 = Re_2 = 300$. Comparison of mean and rms values of u^* for three grids with $G_1 = 297{,}578$ (red line), $G_2 = 1{,}064{,}960$ (green line) and $G_3 = 1{,}414{,}512$ (blue line) nodes, respectively. Results are presented for an x location corresponding to $x = -(L_m/2 + L_e/5)$. (a) and (b) show profiles as a function of y^* at $z^* = 0$. (c) and (d) show profiles as a function of z^* at $y^* = 0.5$. (e) and (f) show profiles as a function of z^* at $y^* = -0.5$. (For interpretation of the references in color in this figure legend, the reader is referred to the web version of this article.)

ues flowing along the length of its channel. In this way, one stream of combined channel flows emerges from the top-right of the top channel, and a second emerges from the bottom-left of the bottom channel. The velocity profiles of the flows at the inlet planes may be symmetric (see Figs. 5a and b) or anti-symmetric (see Fig. 5c) with respect to the z-coordinate direction. When they are anti-symmetric, the inlet velocity profiles are here taken to be shaped as skewed parabolas. Thus, for example, with reference to Fig. 5c, if the velocity profile at one inlet plane has its maximum displaced towards one of the side walls, the velocity profile at the other inlet plane has its maximum displaced towards the opposite side wall.

Earlier flow visualization results from Humphrey and Li (1981), discussed above, and present numerical calculations show that, irrespective of the inlet velocity profile shapes, when fluid motion in this counter-flow configuration is impulsively started from rest, the flow in the shared space region between the edges of the two splitter plates (meaning in the volume defined by $H \times W \times L_m$, approximately) is

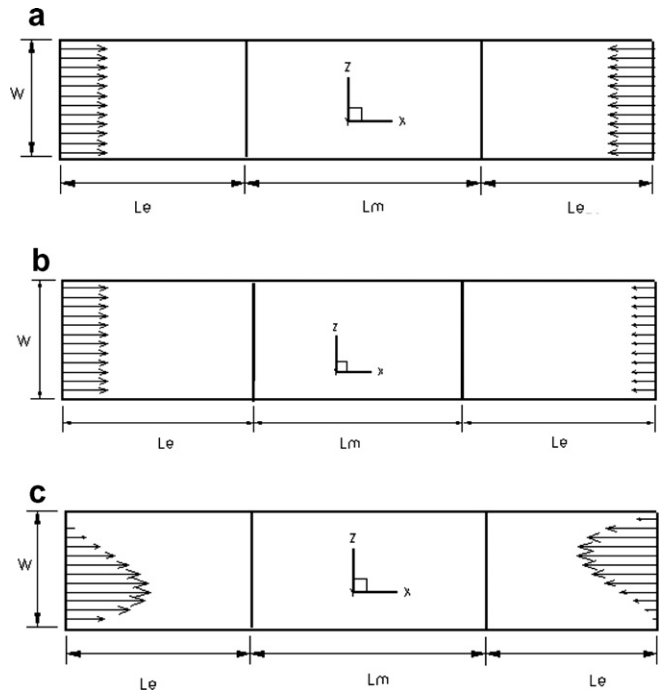

Fig. 5. Top (x–z plane) views of the calculation domain for: (a) *Case 1*: symmetric flow inlet velocity profiles with $Re_1 = Re_2 = 300$; (b) *Case 2*: symmetric flow inlet velocity profiles with $Re_1 = 2 \times Re_2 = 300$; (c) *Case 3*: anti-symmetric inlet velocity profiles for three sub-cases with $Re_1 = Re_2 = 100$, 200 and 300.

initially 2D in x–y planes normal to the z-coordinate direction. It is also initially devoid of vorticity because the flow starting from rest is itself devoid of vorticity. Consequently, the bulk of the flow in the shared space region removed from solid surfaces is initially irrotational. The impulsively started channel flows oppose each other so that the resulting velocity field in the shared space region presents the appearance of a 2D saddle point when viewed in x–y planes normal to the z-coordinate direction (Fig. 2a). It is important to note that the saddle point nature of the flow in this region (and the strain field associated with it) is a feature that persists at later times, even when fluid motion subsequently becomes 3D and vortical. This finding is supported by flow visualization observations (Figs. 2 and 3) and by the calculations shown in, for example, Figs. 6a and b discussed below.

Because of the structure of the saddle point flow, the ω_z component of vorticity generated along the top and bottom surfaces of the splitter plates never penetrates the bulk of the shared space region between the two streams. It is simply convected around the edge of each splitter plate and washed downstream, away from the shared space region. The ω_z component of vorticity generated along the top wall of the top channel and the bottom wall of the bottom channel is also of no consequence, as it is convected along the length of each channel, away from the shared space region.

The conservation equations for ω_x and ω_y are (Tennekes and Lumley, 1972)

$$\frac{\partial \omega_y}{\partial t} + u_x \frac{\partial \omega_y}{\partial x} + u_y \frac{\partial \omega_y}{\partial y} + u_z \frac{\partial \omega_y}{\partial z} = \omega_x \frac{\partial u_y}{\partial x} + \omega_y \frac{\partial u_y}{\partial y} + \omega_z \frac{\partial u_y}{\partial z} + \nu \left(\frac{\partial^2 \omega_y}{\partial x^2} + \frac{\partial^2 \omega_y}{\partial y^2} + \frac{\partial^2 \omega_y}{\partial z^2} \right) \tag{1a}$$

$$\frac{\partial \omega_x}{\partial t} + u_x \frac{\partial \omega_x}{\partial x} + u_y \frac{\partial \omega_x}{\partial y} + u_z \frac{\partial \omega_x}{\partial z} = \omega_x \frac{\partial u_x}{\partial x} + \omega_y \frac{\partial u_x}{\partial y} + \omega_z \frac{\partial u_x}{\partial z} + \nu \left(\frac{\partial^2 \omega_x}{\partial x^2} + \frac{\partial^2 \omega_x}{\partial y^2} + \frac{\partial^2 \omega_x}{\partial z^2} \right). \tag{1b}$$

Because initially $\omega_z = 0$ and $u_z = 0$ in the shared space region, and because initially we also expect $\partial^2/\partial z^2 \gg \partial^2/\partial x^2$ and $\partial^2/\partial z^2 \gg \partial^2/\partial y^2$ adjacent to the vertical side walls in this region, Eqs. (1a) and (1b) simplify to

$$\frac{\partial \omega_y}{\partial t} + u_x \frac{\partial \omega_y}{\partial x} + u_y \frac{\partial \omega_y}{\partial y} = \omega_x \frac{\partial u_y}{\partial x} + \omega_y \frac{\partial u_y}{\partial y} + \nu \left(\frac{\partial^2 \omega_y}{\partial z^2} \right) \tag{2a}$$

$$\frac{\partial \omega_x}{\partial t} + u_x \frac{\partial \omega_x}{\partial x} + u_y \frac{\partial \omega_x}{\partial y} = \omega_x \frac{\partial u_x}{\partial x} + \omega_y \frac{\partial u_x}{\partial y} + \nu \left(\frac{\partial^2 \omega_x}{\partial z^2} \right). \tag{2b}$$

Note that if in Eqs. (1) and (2) x is scaled with L_m, y with $H/2$, z with W, the velocity components with U (a channel inlet flow velocity), and t and the vorticity components with W/U, the dimensionless groups L_m/W, $(H/2)/W$ and Re appear. In this study $L_m/W = 1.5$, $(H/2)/W = 0.76$, and $Re = 100$, 200, 300.

At the start of motion there is no mechanism for the direct generation of the ω_x component of vorticity, and the initial vorticity dynamics in the shared space region is dominated by the ω_y component which is generated along the vertical side walls of the channels (the x–y planes at $z = \pm W/2$). Thus, it follows from Eq. (2a) that the initial time variation of ω_y in the shared space region is due to three primary simultaneous effects: (i) diffusion of ω_y away from the channel side walls, where it is generated; (ii) convection of ω_y along the side walls into the shared space region; (iii) stretching of ω_y in the shared space region by the strain $\partial u_y/\partial y$ associated with the saddle point flow. However, it follows from Eq. (2b) that as the ω_y component of vorticity grows in the shared space region the tilting of ω_y by the strain $\partial u_x/\partial y$ generates the ω_x component. It is then easy to see from the corresponding transport equation for ω_z that tilting of the ω_x and ω_y components of vorticity will, in turn, generate the ω_z component so that the flow in the shared space region has the potential for ultimately becoming unsteady, 3D, and multiscale.

The vertical side walls of both channels contribute to the balance of ω_y in the shared space region. Each channel inlet passage generates ω_y with opposite signs at its two side walls, and because the two channel inlet streams are opposed, the sign of ω_y along a side wall in one channel inlet is opposite to that on the same wall in the other channel inlet. Earlier experiments and present numerical calculations show that the imposition of symmetric inlet plane velocity profiles results in a stable arrangement of coun-

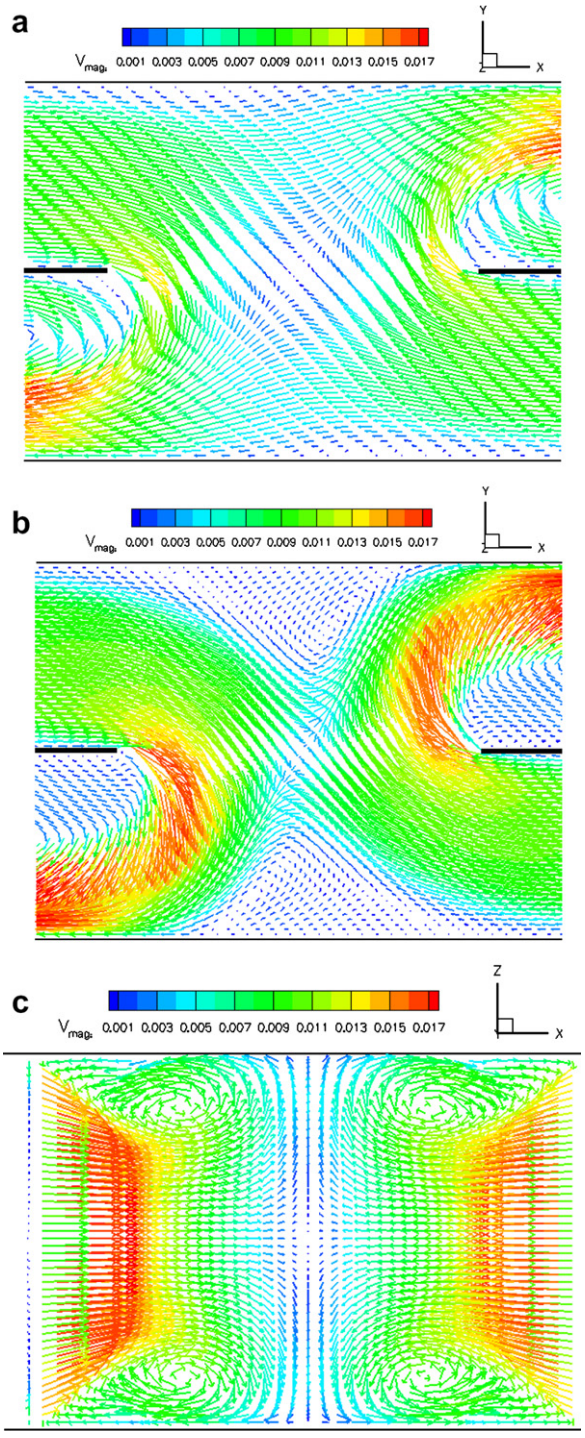

Fig. 6. Calculated vector velocity fields color coded for velocity magnitude for Case 1: (a) Side (x–y plane at $z = 0$) view at $t = 12.5$ s after starting motion from rest. The opposing streams bifurcate to create a saddle point flow. (b) Side (x–y plane at $z = 0$) view at $t = 100$ s. The saddle point nature of the flow persists at this plane. (c) Top (x–z plane at $y = 0$) view at $t = 31.25$ s. The flow has attained a stable, steady (or quasi-steady) condition consisting of two pairs of counter-rotating vortices.

ter-rotating vortices in the shared space region. If, however, the inlet profiles are modified so that they are anti-symmetric in the sense discussed above, the flow in the shared space region ends up being dominated by an anti-symmetric pair of co-rotating vortices which orbit around each other and ultimately merge. Whether the merged pair forms a stable or unstable vortical structure under the influence of the strain field associated with the saddle point flow depends on the values of Re_1 and Re_2.

3. Numerical procedure

Fluid motion in the calculation domain is described by continuity and momentum conservation equations appropriate to an unsteady, 3D, constant property flow expressed in Cartesian coordinates (Bird et al., 2002). The numerical calculations are performed using the FAHTSO code of Rosales et al. (2000,2001). This procedure solves finite difference forms of the conservation equations in dimensional form derived from control volume formulations on staggered grids for pressure and the three velocity components. Convection and diffusion terms are discretized using a third-order quadratic upwind interpolation scheme and a second-order central differencing scheme, respectively. A fully implicit second-order scheme is used for time. The procedure employs the SIMPLE algorithm (Patankar, 1980) in combination with the modified strongly implicit procedure (Schneider and Zedan, 1981) to solve the system of algebraic finite difference equations. For all the calculations performed in this investigation the no-slip boundary condition is imposed at all solid surfaces, and a developed flow condition is prescribed at the channel exit planes. The velocity conditions specified at the channel inlet planes distinguish the cases explored, discussed further below. Physical properties for water at 25 °C are used.

Prior to calculating the flow cases of interest to this investigation, we have performed an assessment of the grid dependence of the numerical results. For this we have calculated the most unsteady and multiscale flow case (corresponding to Case 3, below, with $Re_1 = Re_2 = 300$) on three grids using a time step set to 2.5×10^{-2} s. Given that the highest frequencies with significant energy in this flow are 1 Hz or less, this time step is deemed to be sufficiently small. The (x, y, z) grids employed are equally spaced in the three coordinate directions and consist of $G_1 = (191 \times 41 \times 38)$, $G_2 = (256 \times 80 \times 52)$ and $G_3 = (282 \times 88 \times 57)$ nodes covering the entire $L \times H \times W$ calculation domain. These grids yield control volume resolutions corresponding to 3.5 mm^3, 1.0 mm^{3}and 0.73 mm^3, respectively. In comparison, from the field results obtained for this test case (see for example, the vector plot time sequence shown in Fig. 10) we estimate that the smallest volumetric scales of motion are 2.0 mm^3 or larger. (Note that this estimate is based on full-grid vector plots. For purposes of legibility, in the vector plots shown here only every fourth vector is drawn.)

The accurate calculation of velocity gradients in the boundary layers developing along the walls of the inlet sections and, to a smaller extent, the exit sections of the two channels, but especially $\partial u_x/\partial z$ along the side walls $z = \pm W/2$ of the inlet sections, is crucial to the calculation

accuracy of the ensuing events observed. For this reason, for these three grids, we have calculated mean and rms values of u^* ($\equiv u_x/U$; $U = U_1 = U_2$) from time records spanning the time interval $t = 12.5$–25.0 s after the start of motion from rest. The results obtained are compared at two streamwise locations corresponding to $x = -(L_m + L_e)/2$ and $x = -(L_m/5 + L_e/2)$ along the inlet section of the top channel. These two locations correspond to distances of $0.50 \times L_e$ and $0.80 \times L_e$ measured from the inlet plane of the top channel, and at both of them the mean and rms of u^* have been plotted both in the inlet section of the top channel ($0 \leqslant y^* \leqslant 1$) and the exit section of the bottom channel ($-1 \leqslant y^* \leqslant 0$). In the plots $y^* = y/(H/2)$ and $z^* = z/(W/2)$. The results for $x = -(L_m/5 + L_e/2)$ are provided in Fig. 4 and, by and large, especially for the developing inlet flows, they show relatively small differences between grids G_2 and G_3. The results for $x = -(L_m + L_e)/2$ (not plotted) show even better agreement between these two grids.

Energy spectra corresponding to Case 3 with $Re_1 = Re_2 = 200$ and 300 have also been generated from post-transient flow time records obtained for u^{*2} at location (0, 0, 0) for each of the three grids. The records were processed by means of a MATLAB FFT program. Their length was in excess of 200 s and they were sampled at intervals of 0.025 s allowing frequencies in the range 0.005–10 Hz to be accurately determined. The (0, 0, 0) location, corresponding to the geometrical center of the shared space region, was chosen after checking that frequency spectra obtained at other points in the shared space region revealed the same basic characteristics. The spectra (not plotted) for all three grids, but especially for grids G_2 and G_3, are in good agreement in that they all reveal the same frequencies with significant energy content, and similar energy levels at these frequencies. (Further below we discuss spectra obtained using grid G_2 for Case 3 with $Re_1 = Re_2 = 100$, 200, 300 using the procedure described above applied to time records also exceeding 200 s.)

As a consequence of the grid dependence exploration conducted, the bulk of the calculations of this study have been performed using grid G_2. We recognize that the calculations on this grid for Case 3 with $Re_1 = Re_2 = 300$ are not perfect, but to generate completely grid-independent results would have required computer resources and calculation times beyond our current capabilities. However, the tests performed for this case, the most difficult of the flow cases examined, and the very good qualitative agreement obtained with the flow visualization results of Humphrey and Li (1981), discussed below, show that the calculations on grid G_2 correctly capture all the physics while providing detailed images of the flow not previously available.

4. Calculated results

Calculations have been performed for the computational domain illustrated in Fig. 1, using the dimensions corresponding to the experimental test section of Humphrey and Li (1981), given above. The cases considered, illustrated schematically in Fig. 5, are:

Case 1: Symmetric (plug) flow inlet velocity profiles with $Re_1 = Re_2 = 300$ (Fig. 5a).
Case 2: Symmetric (plug) flow inlet velocity profiles with $Re_1 = 2 \times Re_2 = 300$ (Fig. 5b).
Case 3: Anti-symmetric (skewed-parabolic) inlet velocity profiles, of the form $u_x = f(z)$ for all y, for three sub-cases: $Re_1 = Re_2 = 100$, 200 and 300 (Fig. 5c).

In the experiment of Humphrey and Li (1981) a contracting flow section was used to condition the channel inlet velocity profiles. As a consequence, the inlet velocity profiles specified for Cases 1 and 2 correspond very closely to the experimental. For Case 3 there is a difference in that the skewed-parabolic inlet velocity profiles represent smoothed approximations to the stepwise distributions that were imposed experimentally by partially blocking the flows at each of the two channel inlet planes anti-symmetrically.

Because of the developing nature of the opposed flows in the inlet channel segments, there are no clear-cut characteristic velocity and vorticity scales by means of which to normalize the velocity and vorticity in the shared space region of the counter-flowing streams. As a consequence, field plots of the velocity magnitude and the vorticity components provided in the figures are given in units of m/s and s^{-1}, respectively. Notwithstanding, for reference we note that, for $Re = 300$, the characteristic maximum velocity scale for the fully developed flow in a channel with the height ($H/2$) and width (W) dimensions of interest here, and the associated vorticity scale, are $U = 0.013$ m/s and $\omega(\equiv U/(W/2)) = 0.52\ s^{-1}$, respectively.

4.1. Case 1

A schematic illustrating the top view of this case and the shapes of the inlet plane velocity profiles is shown in Fig. 5a. Side (x–y plane) views of the calculated vector velocity field are shown in Figs. 6a and b at 12.5 s and 100 s, respectively, the latter time corresponding to fully developed flow. (Note that, for figure legibility, in these and subsequent vector plots only every fourth vector is shown.) Fig. 6a illustrates the initial saddle point nature of the flow and Fig. 6b demonstrates its persistence at long times. Fig. 6c shows the formation of two pairs of counter-rotating vortices in the x–z plane at $y = 0$ at $t = 31.25$ s, the appearance of the flow at later times being very similar. Fig. 7 shows plots of the vorticity components also at $t = 31.25$ s. Fig. 7a shows the ω_y component of vorticity in the x–z plane at $y = 0$. Fig. 7b shows the ω_y component of vorticity in an x–y plane passing through the centers of a pair of opposed counter-rotating vortices. Figs. 7c and d show the corresponding fields for the ω_x and ω_z components of vorticity in the same x–z plane. Clearly, ω_y is the dominant component of vorticity in the shared space

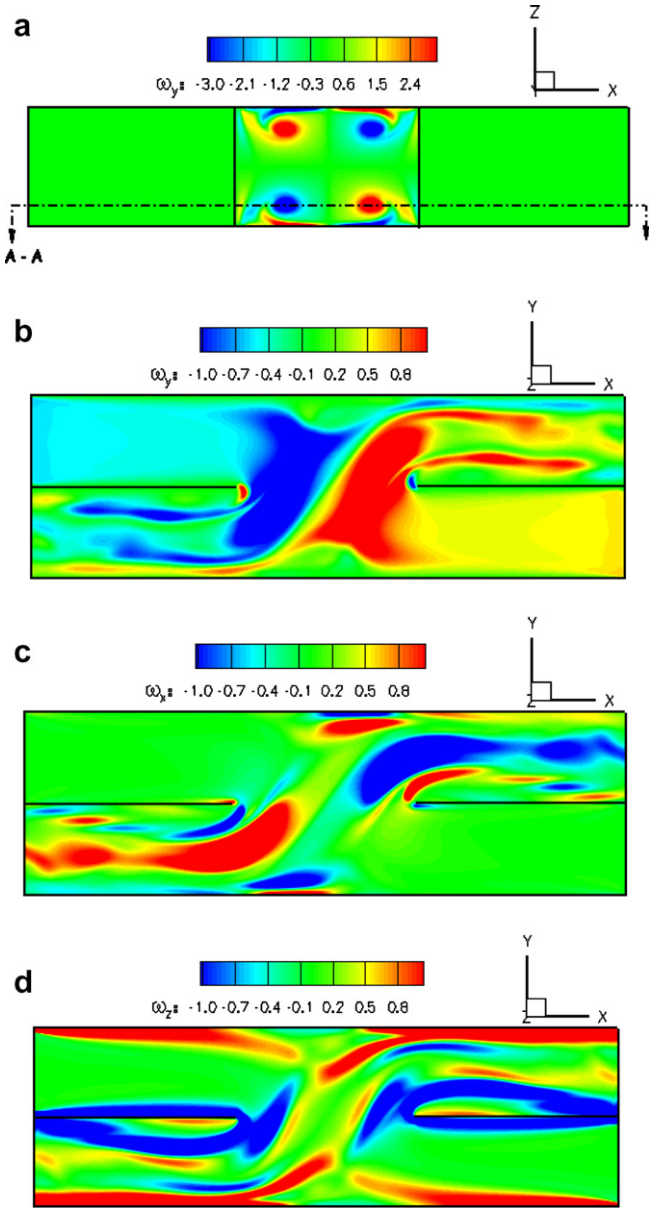

Fig. 7. Calculated vorticity fields for Case 1 at $t = 31.25$ s after starting motion from rest: (a) Top (x–z plane at $y = 0$) view of the ω_y vorticity field corresponding to (Fig. 6c). (b) Side (x–y plane) view of the ω_y vorticity field corresponding to Section A–A in (a). (c) Side (x–y plane) view of the ω_x vorticity field corresponding to Section A–A in (a). (d) Side (x–y plane) view of the ω_z vorticity field corresponding to Section A–A in (a).

region and, between them, ω_x and ω_y define four transverse S-shaped vortices. For Case 1 the flow evolves to a stable, steady (or quasi-steady) state.

4.2. Case 2

A schematic illustrating this case is shown in Fig. 5b. As for Case 1, Figs. 8a and b show that this flow also consists of two pairs of stable, counter-rotating vortices; except that, because $Re_1 = 2 \times Re_2$, one pair of vortices is significantly larger than the other (see, also, Fig. 8c). As in Case 1, the predominant transverse vortices are S-shaped and confined to the side walls of the shared space region. For Case 2 the flow also evolves to a stable, steady (or quasi-steady) state.

4.3. Case 3

A schematic illustrating this case is shown in Fig. 5c. In contrast to Cases 1 and 2, after the transient startup phase the flow for Case 3 is stable and steady (or quasi-steady) at $Re_1 = Re_2 = 100$, and stable but periodic (or quasi-periodic) at $Re_1 = Re_2 = 200$. In both of these sub-cases a pair of anti-symmetric co-rotating vortices generated at opposite side walls merge to form a single vortex occupying the bulk of the shared space region. However, when $Re_1 = Re_2 = 300$ the anti-symmetric pair of co-rotating

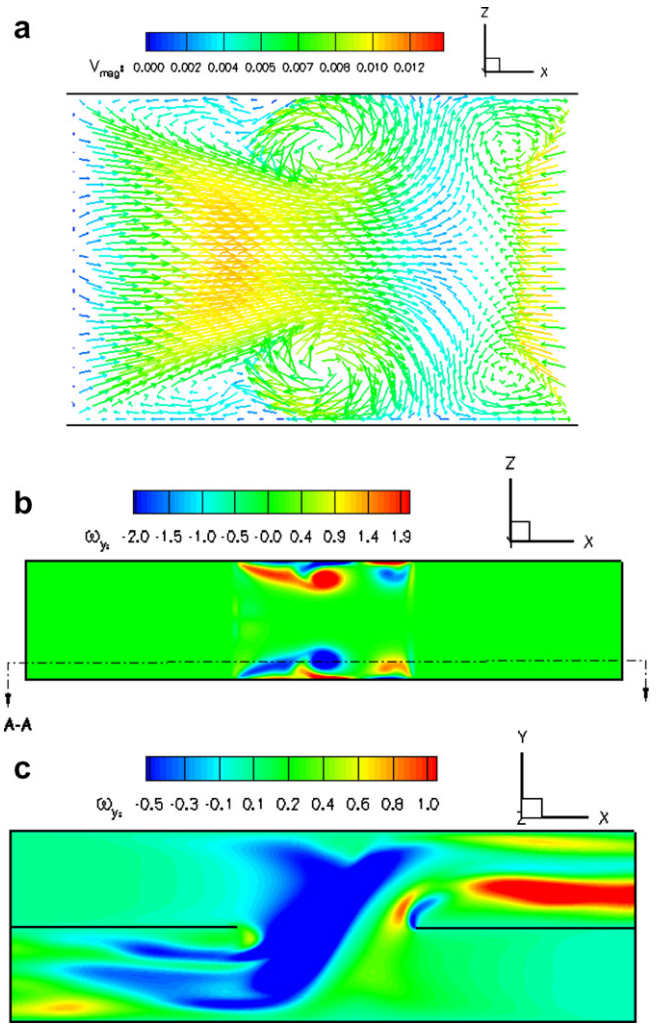

Fig. 8. Calculated velocity and vorticity fields for Case 2 at $t = 31.25$ s after starting motion from rest: (a) Top (x–z plane at $y = 0$) view of the vector velocity field color coded for velocity magnitude. The flow has attained a stable, steady (or quasi-steady) condition consisting of two pairs of counter-rotating vortices, one pair being larger than the other. (b) Top (x–z plane at $y = 0$) view of the ω_y vorticity field corresponding to (a). (c) Side (x–y plane) view of the ω_y vorticity field corresponding to Section A–A in (b).

vortices repeatedly form, orbit, merge and collapse, leading to instances of highly unstable, 3D unsteady flow in the shared space region. We focus here on the results obtained for this sub-case.

Fig. 9a shows the vector velocity field in the x–z plane at $y = 0$, and Figs. 9b–d show the corresponding ω_y vorticity fields in x–z and x–y planes, respectively. Although, as in Cases 1 and 2, each channel flow initially generates two pairs of counter-rotating vortices, because of the skewness of the anti-symmetric inlet plane velocity profiles, an anti-symmetric pair of co-rotating vortices dominates the flow in the shared space region.

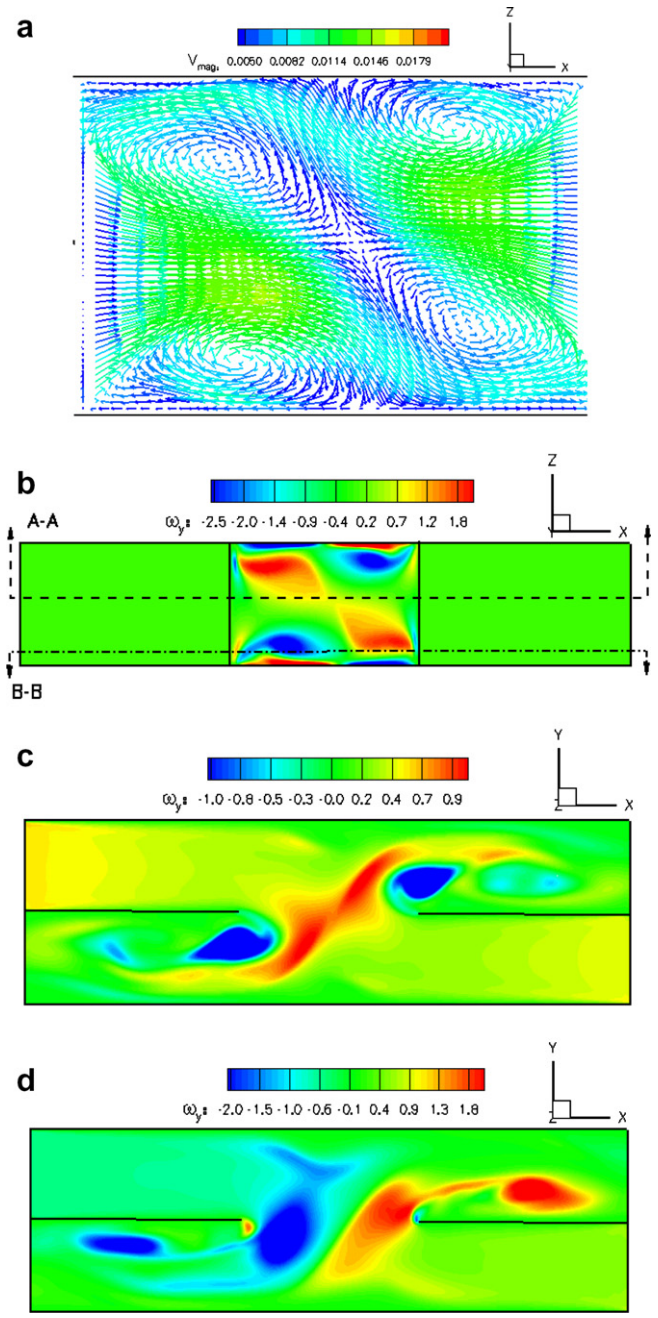

Fig. 9. Calculated velocity and vorticity fields for Case 3 at $t = 18.75$ s after starting motion from rest: (a) Top (x–z plane at $y = 0$) view of the vector velocity field color coded for velocity magnitude. An anti-symmetric pair of co-rotating vortices is observed. The flow is unstable and unsteady. (b) Top (x–z plane at $y = 0$) view of the ω_y vorticity field corresponding to (a). (c) Side (x–y plane) view of the ω_y vorticity field corresponding to Section A–A in (b). (d) Side (x–y plane) view of the ω_y vorticity field corresponding to Sections B–B in (b).

The vector plot time-sequence provided in Fig. 10 illustrates the characteristic evolution of this dominant vortex pair. At $t = 88.75$ s the pair is well defined, being at locations NW and SE, respectively, of a central vortex. Each of the pair of vortices rotates about its axis in the clockwise direction while they both start rotating around the central vortex in the anti-clockwise direction. The pair of vortices orbit around the central core until some instant in time, between $t = 100$ s and $t = 112.5$ s, when they merge and collapse to produce a temporary disorganized state of motion. This cycle is observed to repeat with a periodicity ranging between 50 and 65 s, approximately.

Energy spectra for the above three sub-cases are provided in Fig. 11. The spectra are based on time records of u^{*2} obtained at location (0, 0, 0) in the shared space region after verifying that this location is representative of the spectral energy content of the flow. The time records analyzed exclude the initial transient and in each case cover a time interval ranging from 45.2 s after starting the flow from rest to 250 s. The spectra show that the bulk of the energy in these flows lies at frequencies $f < 1$ Hz, and that it increases significantly and extends to higher frequencies with increasing Reynolds number.

5. Discussion

The vortical motion of a fluid in the shared space region of a counter-current parallel channels shearing flows configuration with $L_m/W \approx (H/2)/W \approx 1$ is stable for symmetric inlet plane velocity profiles, irrespective of factor-of-two ratios in the bulk average velocities through the two channels (Cases 1 and 2). However, the same is not true for anti-symmetric inlet plane velocity profiles where the formation, merging and collapse of a pair of dominant anti-symmetric co-rotating vortices takes place repeatedly (Case 3 when $Re_1 = Re_2 = 300$). The question arises as to why this should be the case and we believe the answer lies primarily in the vortex stretching terms $\omega_y \partial u_y/\partial y$ and $\omega_x\ \partial u_x/\partial x$ in Eqs. (2a), (2b). We suggest that, for large enough Reynolds numbers in Case 3, (i) the generation and simultaneous amplification (by stretching) of the ω_y and ω_x components of vorticity in the shared space region occurs at a faster rate than these components can be removed by convective transport and, (ii) because these components cannot increase in magnitude indefinitely, (iii) the flow becomes rotationally unstable and breaks down. The lack of directionality in the ensuing phase of disorganized motion allows a 'cleaning up' of the shared space region by the background base flow and the cycle repeats.

The structure of the flow resulting from the repeated breakdown of the merging vortex pair in the case with

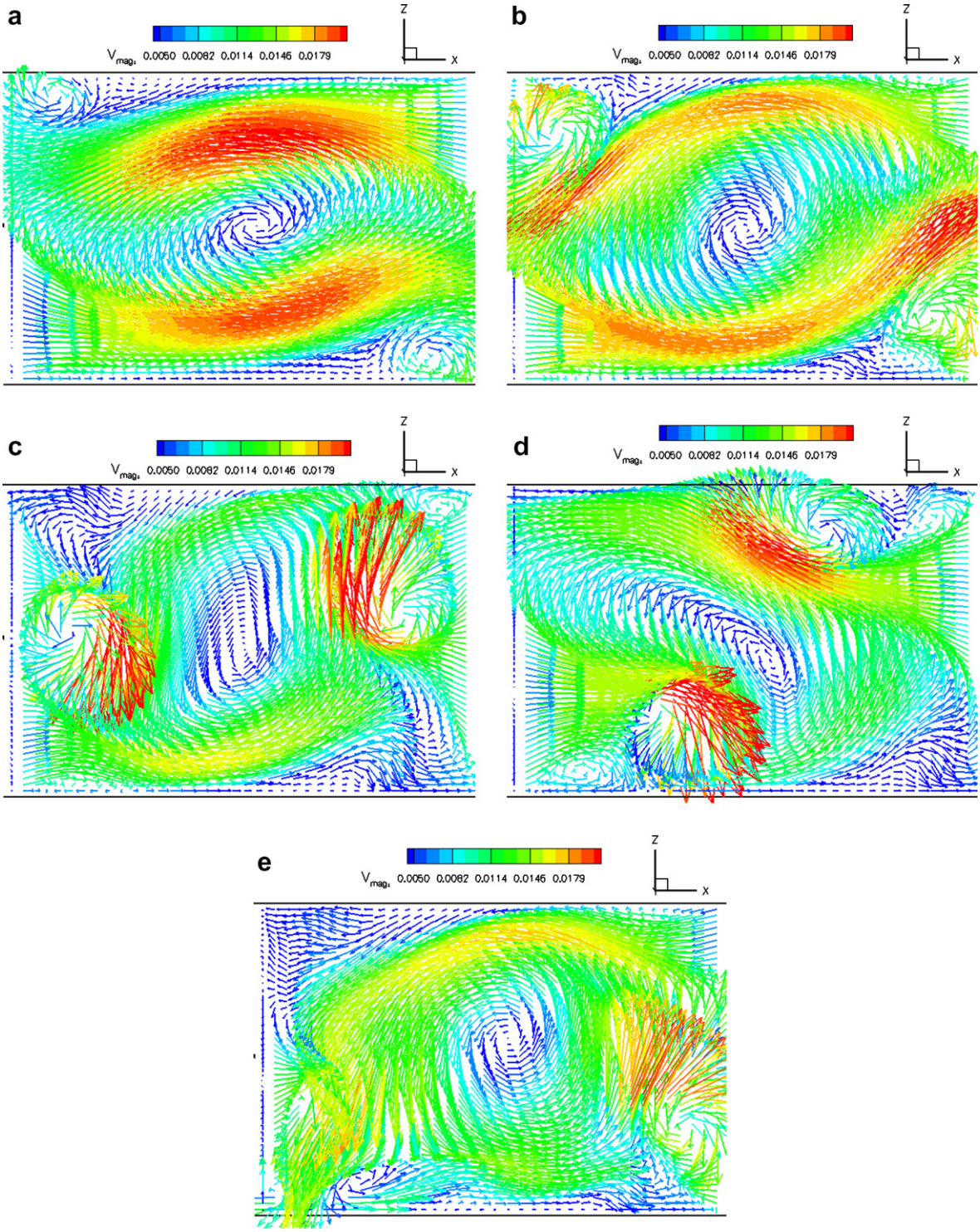

Fig. 10. Calculated vector velocity fields color coded for velocity magnitude illustrating the time evolution of the flow for Case 3 (x–z plane at $y = 0$) at times: (a) $t = 88.75$ s; (b) $t = 93.75$ s; (c) $t = 97.5$ s; (d) $t = 100$ s; (e) $t = 112.5$ s. The sequence of images illustrates the formation, merging and collapse of a dominant pair of anti-symmetric co-rotating vortices that originate in the top-left (NW) and bottom-right (SE) corners of the plane viewed. Both vortices rotate in the clockwise direction about their respective axes while orbiting in the counter-clockwise direction around a center vortex in the plane viewed. Between $t = 100$ s and 112.5 s the vortex pair merge and collapse to produce a temporary disorganized state of motion in the shared space region.

anti-symmetric inlet plane velocity profiles (Case 3 with $Re_1 = Re_2 = 300$) is characterized by a range of relatively energetic scales of motion typical of a disorganized, chaotic (but non-turbulent) flow. Spectra of u^{*2} and v^{*2} obtained at (0, 0, 0) and other locations (not plotted) in the shared space region show that most of the motion energy is associated with frequencies below 1 Hz, approximately. In this regard, two frequency ranges are particular noteworthy.

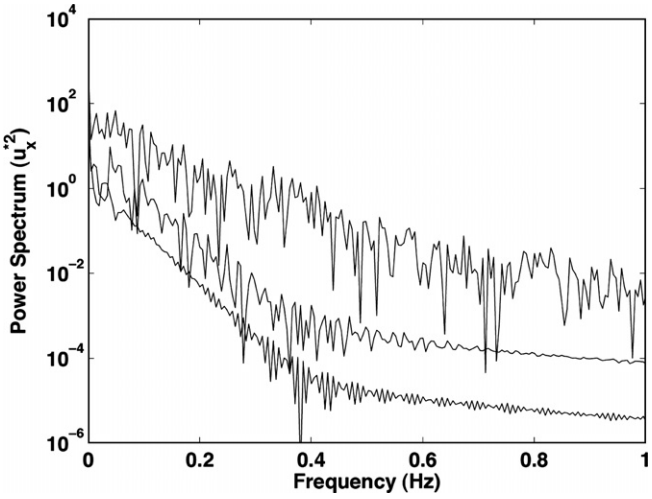

Fig. 11. Spectra of u^{*2} at location (0, 0, 0) for Case 3 with: $Re_1 = Re_2 = 300$ (top curve); $Re_1 = Re_2 = 200$ (middle curve); and $Re_1 = Re_2 = 100$ (bottom curve).

One, spanning 0.05–0.1 Hz, approximately, is attributed to the orbiting vortex pair. The other, spanning 0.015–0.02 Hz, approximately, is attributed to the repeated collapse of the merging vortex pair in the shared space region. The associations between these two frequency ranges and the vortical motions responsible for them have been arrived at by careful inspection of animations produced of the calculated flows. The dimensionless frequency, fW_f/U, associated with the repeated collapse of the merging vortex pair ranges between 0.07 and 0.1 and is in reasonable agreement with the experimental observations of Humphrey and Li (1981) where it ranges from 0.03 to 0.07, approximately, for $Re = 300$.

In an effort to better understand the behavior of Case 3 we have generated plots of $u^*(t + \Delta t)$ versus $u^*(t)$, of $v^*(t + \Delta t)$ versus $v^*(t)$, and of $v^*(t)$ versus $u^*(t)$ for the sub-cases corresponding to $Re_1 = Re_2 = 100$, 200 and 300 for total times of 250 s including the initial flow transient. At all Reynolds numbers the plots of $u^*(t + \Delta t)$ versus $u^*(t)$ and of $v^*(t + \Delta t)$ versus $v^*(t)$ (not shown here) display the characteristic shapes of sinusoidal-like oscillations. In contrast the plots of $v^*(t)$ versus $u^*(t)$ (shown in Fig. 12) display very different patterns. At time zero $v^*(t) = u^*(t) = 0$ and, thereafter, the $v^*(t) - u^*(t)$ pair describe orbits the shapes of which depend on the values of $Re_1 = Re_2$. For $Re_1 = Re_2 = 100$ the orbit eventually settles to a steady or quasi-steady fixed point state corresponding to $v^*(t) = -0.167$ and $u^*(t) = 0.258$. For $Re_1 = Re_2 = 200$ the orbit consists of a series of patterns, each similar in shape to the orbit observed for $Re_1 = Re_2 = 100$, that repeat in variously distorted forms as a function of time. Because this case corresponds to a periodic or quasi-periodic flow, the orbit never converges to a final fixed point state. For $Re_1 = Re_2 = 300$ there is no recognizable repeating pattern in the $v^*(t) - u^*(t)$ orbit which has a chaotic appearance.

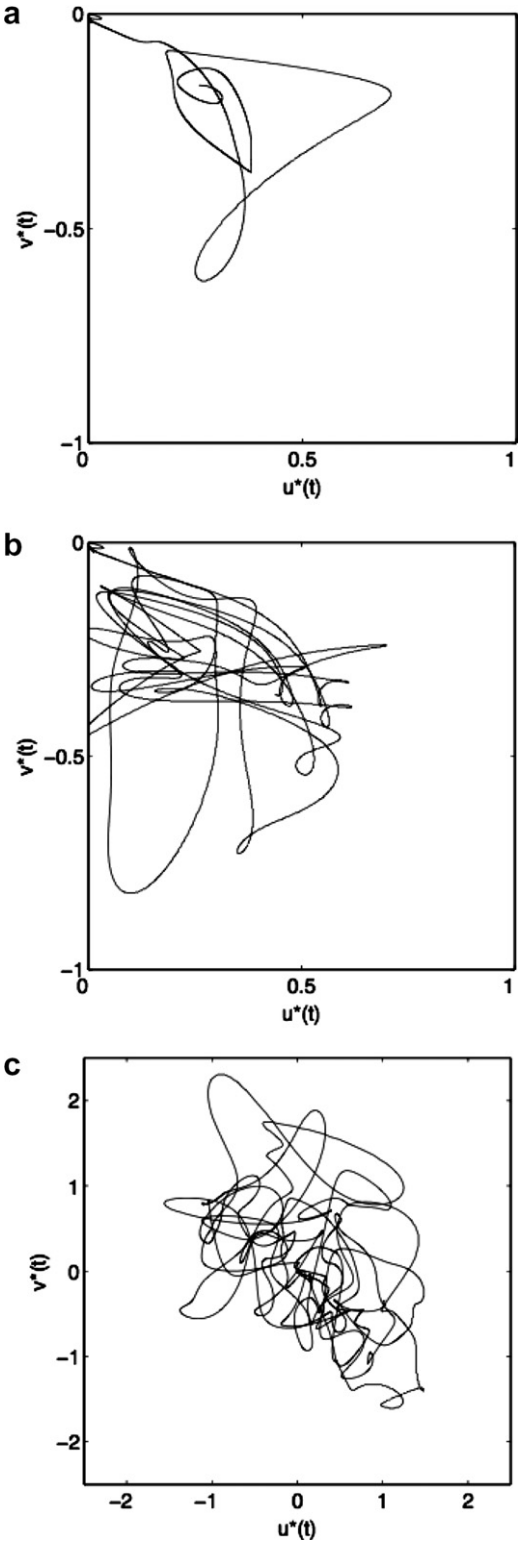

Fig. 12. Plots of $v^*(t)$ versus $u^*(t)$ at location (0, 0, 0) for Case 3 with: (a) $Re_1 = Re_2 = 100$; (b) $Re_1 = Re_2 = 200$; and (c) $Re_1 = Re_2 = 300$.

To help interpret the results in Fig. 12, we note that the spectra for u^{*2} and v^{*2} display slightly different fundamental frequencies for frequencies larger than 0.049 Hz. Consider, therefore, two purely sinusoidal velocity component oscil-

lations described by $u^*(t) = A \sin(\omega_u t + \phi_u)$ and $v^*(t) = B \sin(\omega_v t + \phi_v)$.[1] Let $U^*(t) = u^*(t)/A$, $V^*(t) = v^*(t)/B$, $\omega_v = \omega_u + \Delta\omega$, and $\phi_v = \phi_u + \Delta\phi$. It follows that $V^*(t) = U^*(t)\cos(\Delta\omega t + \Delta\phi) \pm \sqrt{1 - U*(t)^2}\sin(\Delta\omega t + \Delta\phi)$ with the sign of the second term on the right hand side of this expression given by the sign of $\cos(\omega_u t + \phi_u)$. If both $\Delta\omega t \to 0$ and $\Delta\phi \to 0$ then $V^*(t) = U^*(t)$, a straight line. If $\Delta\omega t \to 0$ and $\Delta\phi \neq 0$ the orbit described by the $V^*(t) - U^*(t)$ pair is elliptical, never crossing itself. If $\Delta\omega t \neq 0$ (regardless of the value of $\Delta\phi$) the orbit is a complex curve that crosses itself at various points in the $V^*(t) - U^*(t)$ plane. The conclusion is that it is necessary for $\Delta\omega t \neq 0$ for the orbit to cross itself in the $V^*(t) - U^*(t)$ plane and since this is true for $t > 0$ it is necessary for $\Delta\omega \neq 0$ for orbit crossings to occur.

From these observations we conclude that between $Re_1 = Re_2 = 100$ and $Re_1 = Re_2 = 200$ small quasi-regular perturbations affect the frequency dependencies of $u^*(t)$ and $v^*(t)$ leading to orbit crossings in the $v^*(t) - u^*(t)$ plane that display some degree of regularity because of the periodic (or quasi-periodic) nature of the flow. However, between $Re_1 = Re_2 = 200$ and $Re_1 = Re_2 = 300$ the perturbations become irregular and large enough to produce $v^*(t) - u^*(t)$ orbits of chaotic appearance. For $Re_1 = Re_2 = 100$ the fixed point state acquired by the flow at location (0, 0, 0) is $v^*(t) \neq 0$ and $u^*(t) \neq 0$ when, in fact at this location we would expect $v^*(t) = 0$ and $u^*(t) = 0$ by symmetry. However, it is only when $Re_1 = Re_2 = 300$ that u^* and v^* both vary stochastically around 0. It appears, therefore, that for $Re_1 = Re_2 = 100$ the flow has experienced a symmetry-breaking bifurcation and that for $Re_1 = Re_2 = 200$ it has become time dependent.

6. Applications to mixing

To illustrate the mixing potential of the basic counter-flows configuration investigated in this study (Fig. 1), flow visualization experiments were performed in a counter-current fluid–fluid flows mixer (C^2F^3M) consisting of five basic counter-flow units concatenated in series. In this device, the two exit streams from a basic counter-flow unit are the two inlet streams for the next.

Top (plan) views of the C^2F^3M are shown in Fig. 13a and b. It was fabricated by joining together two pieces of Plexiglass, each of dimensions 10.5 cm × 10 cm × 1.2 cm, into each of which was machined a continuous channel with periodic 180° turns to create the concatenated counter-flow passages. Each of the straight channel sections has a depth of 1 cm, a width of 1.1 cm, and a length of 7.1 cm. The flow passes from one straight channel section into the next by turning 180° through a 0.6 cm gap. A thin sheet of Plexiglass (10.5 cm × 10 cm × 0.025 cm) is sandwiched between the two larger plates and the three pieces are bolted together by corner screws. The sheet has slots cut into it that are 1.1 cm wide and 1.75 cm long, and the slots are centered halfway along the lengths of the straight channel sections to allow the counter-flowing streams to interact. The thickness of the walls separating adjacent straight channel sections is 0.2 cm. The dimensions of the straight counter-flowing sections of the C^2F^3M mixer are scaled to be 1/5, approximately, those of the system investigated by Humphrey and Li (1981).

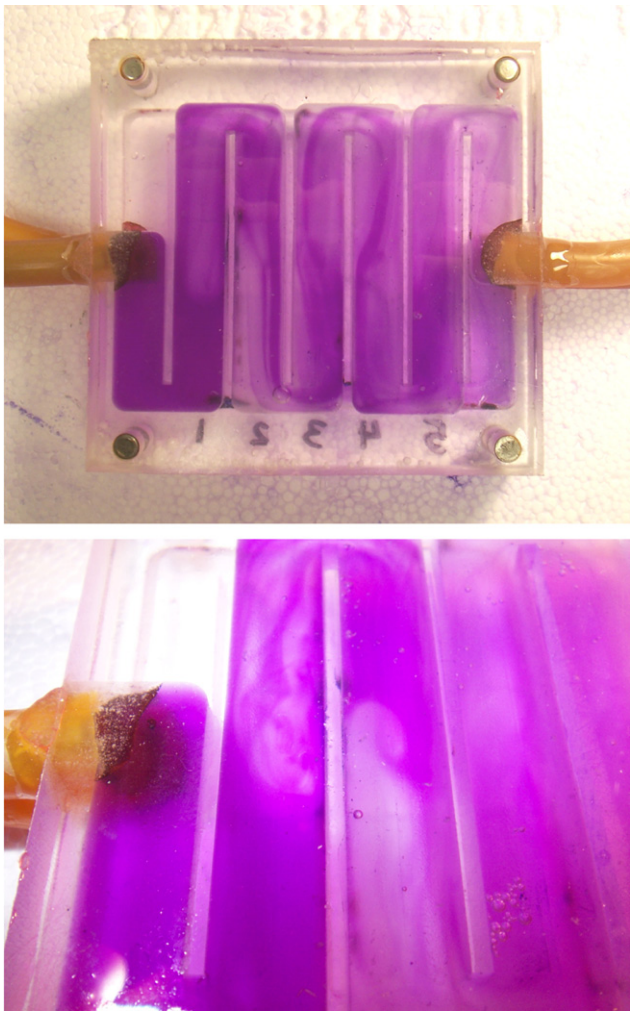

Fig. 13. Top (plan) views of the counter-current fluid–fluid flows mixer (C^2F^3M) formed by concatenating five basic counter-flow units of the type shown in Fig. 1; for dimensions see text. In the figures the basic units are aligned vertically, with the connecting 180° passages at the top and bottom and the two channel inlets at the left. The water stream with gentian violet enters the bottom channel and flows downwards before turning 180° to flow upwards through the first of the five basic units. Correspondingly, the clear water stream enters the top channel and flows upwards before turning 180° to flow downwards through the first of the five basic units. (a) Case with $Re_1 \approx Re_2 \approx 95$, corresponding to quasi-steady flow; (b) Close-up view of the case with $Re_1 \approx Re_2 \approx 160$, corresponding to unsteady, chaotic, flow. (Note that the device has been turned upside down to locate the clear stream over the colored stream.)

[1] Even though the $u^*(t)$ and $v^*(t)$ being considered are the components of a vector velocity at a point in the flow, they can have different frequencies ω_u and ω_v. Such a situation can be set up, for example, in a channel with porous walls where the streamwise and transverse components of velocity are made to oscillate at different frequencies.

Water at ~24 °C was introduced into the inlet sections of the concatenated counter-flowing channel units by means of rubber tubes, and it was similarly removed using rubber tubes attached to the exit sections. The feed tubes were connected to separate constant head reservoirs, one of which had a very small amount of gentian violet in solution to visualize the flow interactions in the C^2F^3M. The rates of flow of the counter-flowing streams were controlled by means of screw-clamps used to compress the feed tubes, and they were determined by means of timed volumetric measurements. In this way, the Reynolds number of the flow in either channel was known to ±5%, approximately.

Still pictures and video recordings of fluid motion in the C^2F^3M were made for flowing streams with $Re_1 \approx Re_2$ in the range 100–1000; Fig. 13 shows typical images for the cases with (a) $Re_1 \approx Re_2 \approx 95$ and (b) $Re_1 \approx Re_2 \approx 160$, respectively. As expected for this range of Reynolds numbers, each channel stream in a basic unit is split in two by the saddle point nature of the flow in the shared space region of the unit, and each of these split streams merges with a corresponding split stream from the other channel. In this way, the streams are split and recombined five times which significantly enhances their mixing. In this range of Reynolds numbers, transverse vortices also appear in the shared space region of the flow in each unit that enhance mixing; the vortices are particularly noticeable in the close-up image of Fig. 13b. At low Reynolds numbers ($Re \leqslant 100$, approximately) the flow in the shared space region of a unit consists of stable core vortex structures, formed by alternating layers of the counter-flowing streams (Fig. 13a). At higher Reynolds numbers ($Re > 150$) the vortical structures formed in the shared space region are unstable and chaotic in appearance (Fig. 13b). Irrespective of whether they are stable or unstable, the vortical structures work to enhance mixing. By construction, in passing from one unit to the next, each channel stream is made to turn 180° which results in additional centrifugally-driven cross-stream secondary motions that also benefits mixing.

In the ranges of the geometrical and dynamical parameters examined, the sum total of the flow visualization results obtained in this device show that the combination of: (i) stream splitting and recombination, (ii) strained vortical structures appearing in the shared space region common to the counter-flowing streams, and (iii) cross-stream secondary motions due to 180° turns, result in essentially complete mixing of the two streams in less than five concatenated basic counter-flow units.

7. Summary and conclusions

Numerical calculations of the motion of a Newtonian fluid in a counter-current shearing flows configuration yield very good qualitative agreement with earlier flow visualization results while allowing a depth of exploration not previously conducted. We summarize here some of our main findings. For symmetric inlet plane velocity profile conditions, the pairs of vortices formed in the shared space region of the flow counter-rotate and are stable and the flow is essentially steady or quasi-steady. For anti-symmetric inlet plane velocity profile conditions, a pair of anti-symmetric co-rotating vortices in the shared space region dominates the flow. This vortex pair is stable and steady (or quasi-steady) or stable and periodic (or quasi-periodic) at low Reynolds numbers, and unstable and dynamically complex at high Reynolds numbers. In the latter case the anti-symmetric vortices first orbit around a core central vortex, then they merge and collapse chaotically due to the strain imposed by the background saddle point flow. Earlier experimental results suggest that this phenomenon repeats with an average frequency that is proportional to the flow Reynolds number. Present analysis and numerical calculations suggest that the generation and amplification of vorticity in the shared space region of the flow occur at a faster rate than vorticity can be removed by convective transport and, because the vorticity in this region cannot increase in magnitude indefinitely, the flow becomes rotationally unstable and breaks down periodically.

This study has been limited to a counter-current channel flows geometry with characteristic length scales L_m, W and $H/2$ such that $L_m/W = 1.5$ and $(H/2)/W = 0.76$ in which the effects of inlet flow Reynolds numbers and inlet velocity profile shapes have been explored. It would be interesting to study the characteristics of this flow over larger ranges of the parameters L_m/W, $(H/2)/W$, Re_1, and Re_2. This could be done numerically, as shown here, or via a stability analysis approach. However, this task is beyond the scope of the present work.

Flow visualization observations in a specially fabricated counter-current fluid–fluid flows mixer, consisting of a concatenated series of basic counter-shearing flows units of the type shown in Fig. 1, show that it has considerable potential for the accelerated mixing of confined fluid streams at both low and large values of the Reynolds number.

Acknowledgements

The authors thank S. Pillapakkam for his assistance with the numerical calculations while he was at the University of Virginia. They also acknowledge helpful discussions held with Oliver O'Reily at the University of California, Berkeley, and Hossein Haj-Hariri at the University of Virginia. Much of this study took place while JACH was a Guest Professor at the University of Vienna for which he is very grateful.

References

Behrens, A.A., Hallberg, M.P., Forliti, D.J., Strykowski, P.J., 2004. Combustion control of premixed/prevaporized JP-10 in air downstream of a backward-facing step using counterflow. In: Advances in Combustion and Noise Control. Cranfield University Press, pp. 99–114, Chapter 7.

Bird, R.B., Stewart, W.E., Lightfoot, E.N., 2002. Transport Phenomena. John Wiley and Sons, Inc., New York.

Forliti, D.J., Behrens, A.A., Tang, B.A., Strykowski, P.J., 2004. Prevaporized JP-10 combustion and the enhanced production of turbulence using countercurrent shear. In: Control of Combustion Processes. CRC Press, pp. 71–82, Chapter 6.

Forliti, D.J., Tang, B.A., Strykowski, P.J., 2005a. An experimental investigation of planar countercurrent turbulent shear layers. J. Fluids Mech. 530, 241–264.

Forliti, D.J., Strykowski, P.J., 2005b. Controlling dump combustor flows using countercurrent shear. J. Fluid Eng. 127, 438–448.

Humphrey, J.A.C., Li, S.K.-K., 1981. Tilting, stretching, pairing and collapse of vortex structures in confined counter-current flow. J. Fluids Eng. 103, 466–470.

Lonnes, S., Hofeldt, D., Strykowski, P., 2001. Flame speed control using a countercurrent swirl combustorAdvances in Chemical Propulsion: Science to Technology, vol. 17. CRC Press, pp. 277–290.

Patankar, S.V., 1980. Numerical Heat Transfer and Fluid Flow. Hemisphere Publishing Corporation, McGraw-Hill Book Company, New York.

Rosales, J.L., Ortega, A., Humphrey, J.A.C., 2000. A numerical investigation of the convective heat transfer in unsteady laminar flow past a single and tandem pair of square cylinders in a channel. Numer. Heat Transfer Part A. 38, 443–465.

Rosales, J.L., Ortega, A., Humphrey, J.A.C., 2001. A numerical simulation of the convective heat transfer in confined channel flow past square cylinders: comparison of inline and offset tandem pairs. Int. J. Heat Mass Transfer 44, 587–603.

Schneider, G.E., Zedan, M., 1981. A modified strongly implicit procedure for the numerical solution of field problems. Numer. Heat Transfer 4, 1–19.

Sudarsan, A.P., Ugaz, V.M., 2006. Multivortex mixing. PNAS 103, 7228–7233.

Tennekes, H., Lumley, J.L., 1972. A First Course in Turbulence. The MIT Press, Cambridge.